PCCP

Accepted Manuscript

ROYAL SOCIETY OF CHEMISTRY

www.rsc.org/pccp

Journal Name

RSCPublishing

ARTICLE

Wurtzite CZTS Nanocrystals and Phase Evolution to Kesterite Thin Film for Solar Energy Harvesting

Cite this: DOI: 10.1039/xoxxoooooox

Received ooth January 2012,
Accepted ooth January 2012

DOI: 10.1039/xoxxoooooox

www.rsc.org/

Uma V. Ghorpade[a,b], Mahesh P. Suryawanshi[a], Seung Wook Shin[c], Chang woo Hong[a], Inyoung Kim[a], Jong. H. Moon[a], Jae Ho Yun[d], Jin Hyeok Kim[a]*, Sanjay S. Kolekar[b]*

[a]*Department of Materials Science and Engineering and Optoelectronics Convergence Research Centre, Chonnam National University, 300, Yongbong-Dong, Buk-Gu, Gwangju 500-757, South Korea*

[b]*Analytical Chemistry and Material Science Research Laboratory, Department of Chemistry, Shivaji University, Kolhapur 416-004, India*

[c]*Center for Nanomaterials and chemical Reactions, Institute for Basic Science, Daejeon 305-701, Korea*

[d]*Photovoltaic Research Group, Korea Institute of Energy Research, 71-2 Jang-Dong, Yuseong-Gu, Daejeon 305-343, South Korea*

Quaternary indium- and gallium-free kesterite (KS)-based compound, Cu_2ZnSnS_4 (CZTS) has received significant attention for their potential applications in low-cost and sustainable solar cells. It is well known that the reaction time, reactivity of the precursors, and types of capping ligands used during colloidal nanocrystals (NCs) synthesis strongly influence the crystallographic phase of the NCs. Here, we demonstrate a non-toxic and green synthetic strategy for both the synthesis of CZTS NCs and the fabrication of highly efficient CZTS absorber layers using an ink formulation without a toxic solvent, which meets the comprehensive framework for green chemistry that covers major aspects of the environmental strain. In particular, pure metastable wurtzite (WZ) CZTS NCs are synthesized using the environmentally benign, polyol-mediated hot-injection technique at a low reaction temperature. The influence of the reaction time on the properties of the CZTS NCs is investigated in detail. Based on detailed reaction-time-dependent phase evolution, a possible growth and formation mechanism is proposed. Furthermore, a scalable, low-cost, binder-free ink formulation process without ligand exchange is developed using ethanol as the dispersal solvent. The as-prepared WZ-derived CZTS NC thin films are observed to undergo a phase transformation to KS during annealing in a S vapor atmosphere via rapid thermal annealing (RTA) above 500 °C, and surprisingly, this process results in fully sintered, compact and uniform CZTS thin films with large-sized grains. The best solar cell device fabricated using a CZTS absorber that was sulfurized at an optimized temperature exhibits the power conversion efficiency (PCE) of 2.44 %, which is the highest efficiency among polyol based HI route.

Keywords: Wurtzite CZTS, phase evolution, a scalable low-cost and binder-free nano ink, green synthesis process, solar energy harvesting

Introduction

Indium- and gallium-free kesterite (KS)-based compound, Cu2ZnSnS4 (CZTS), is of particular interest because of its high absorption coefficients (greater than 10^4 cm^{-1}), low toxicity and suitable band gap for solar energy harvesting.[1-4] Recently, CZTS-NC-based inks have been suggested as a material that would allow for global-scale photovoltaic (PV) applications and have exhibited the promising efficiency of 10.2 %.[5] However, the use of various organic solvents and surfactants, including phosphine oxide, thiols, amines, and hydrazine,

during colloidal synthesis may have various impacts on the environment. Therefore, the use of an ecofriendly and less hazardous organic solvent is required. Additionally, the difficulties are related to the coordinating long chain ligands, surface capping agents, presence in a certain solvent which create stability without accumulation of NCs.[3] However, it affect the optical and electrical properties of material causing the steric hindrances to the electronic movements.[6, 7] Consequently, an environmentally friendly chemical route that avoids inconvenient ligand functional groups is required.

The reported colloidal CZTS-based NCs mostly exhibit stannite or KS structures.[3, 4] Recently, a few research groups reported colloidal WZ CZTS NCs, which are seldom observed in quaternary compounds.[8-11, 32-34] The randomly distributed cations in the WZ crystal phase offer greater flexibility for stoichiometry control and crystal structure, because of which the Fermi energy can be tuned over a wide range.[8] This crystal behavior suggests that it is possible to synthesize KS structured thin films in the WZ phase at lower annealing temperature.[28] Le et al. reported the synthesis of WZ CZTS NCs using a mixture of oleylamine (OLA) and dodecanethiol (DDT) and controlled the crystal structure by adjusting the OLA to DDT ratio.[10] Fan et al. reported the synthesis of WZ CZTS nanorods prepared using mixtures of DDT and triphenylphosphite (TPP), and tunable shapes for CZTS nanorods were achieved by the controlling compositional ratio of Cu/(Zn+Sn).[12] Furthermore, Yang et al. reported 4.3 % efficiency using OLA and DDT after a further selenization process.[34] Although the previous reports were able to synthesize colloidal WZ CZTS with the desired shapes, the synthesis was performed in DDT, OLA, TPP and amine-based toxic solvents at high reaction temperatures.[9-11] These finding collectively contribute to the development of WZ CZTS NCs and the fabrication of CZTS-based thin film solar cells (TFSCs). However, a green and controllable synthesis of WZ CZTS NCs prepared without using toxic chemical would provide a way to develop NCs with exciting new properties for PV applications. This encouraged us to develop a new, robust, cost-effective and green synthetic strategy for the synthesis of CZTS NCs with WZ structure that is scalable and useful for harvesting solar energy.

Here, we developed a synthetic strategy for WZ CZTS NCs using a polyol-based hot-injection (HI) route at low temperature (<200 °C) that employs ethylene glycol (EG) as a green solvent. For further detailed understanding, a reaction-time-dependent study of the phase evolution and formation mechanism of WZ CZTS NCs was proposed. EG is a low-cost and less-toxic solvent that can efficiently complex and stabilize the surfaces of NCs without agglomeration. It functions not only as a complexing agent but also as a spacer to modulate the distance between metal ions, similar to OLA, octadecene (ODE), TPP, etc., which prevent the NCs from aggregating.[13, 14] Moreover, the synthesized NCs require a stable suspension in a suitable solvent for thin film formation. The CZTS NCs capped with OLA, ODE or TPP are hydrophobic, and they can only be dispersed in an organic solvent (such as toluene and hexanethiol), which are not environmentally benign.[3] Unfortunately, few studies have focused on green and sustainable solvent for the preparation of WZ-CZTS-based NC ink.[15, 16] This lack of appropriate solvent motivated us to introduce an alternative, eco-friendly, binder-free WZ-CZTS-NCs-based ink formulation that utilizes ethanol as a dispersal solvent. This new solution can be formatted into dense, micro-structured CZTS precursor thin films with low C concentration. Thus, CZTS-based TFSCs can be fabricated using green processes. Furthermore, to clarify the phase evolution of WZ-derived CZTS-NCs-based precursor thin films to KS CZTS thin films, the WZ-derived CZTS NCs films were annealed in a graphite box under a non-toxic, Se-free S vapor atmosphere using an RTA process at different temperatures. In addition to the basic studies on WZ CZTS NCs and their phase evolution to a KS CZTS absorber layer, the photovoltaic performances of KS CZTS-based TFSCs were evaluated.

Experimental Section

Synthesis of CZTS NCs

In a typical synthesis, stoichiometric amounts of the metal precursors were dissolved in EG in a three-neck flask with constant magnetic stirring. The sulfur source was synthesized by dissolving thiourea into a separate EG solution and hot injected into the metal precursor solution at 130 °C. The flask was purged with Ar for 10 min, and the reaction was allowed to remain at the optimized temperature of 190 °C. Aliquots were taken at reaction times of 1 h, 2 h, 3 h and 4 h. The resulting NCs were further used for thin film formation. The details of the synthetic procedure, characterization, ink formulation and device fabrication are explained in the Electronic Supplementary Information (ESI).

Results and Discussion

Synthesis of phase pure metastable WZ CZTS NCs

Figure 1a shows powder-X-ray diffraction (PXRD) patterns of WZ CZTS NCs at various reaction times. All of the as-synthesized NCs exhibit broad peaks at 2θ =26.89, 28.21, 30.40, 39.37, 47.45, 51.30 and 56.22°, which correspond to the (1 0 0), (0 0 2), (1 0 1), (1 0 2), (1 1 0), (1 0 3) and (1 1 2) diffraction planes, respectively, of the CZTS WZ phase.[10] The relative widths of these primary peaks increase with reaction time, which could be due to the changes in the crystal structure. In addition, several peaks at 2θ = 22.9, 25.9, 32.9, 40.8, 52.96°, etc. are observed at 1 h and 2 h, which correspond to the secondary phases of $Cu_{2-x}S$, $Sn_{1-x}S_x$ and Cu_2SnS_3. (JCPDS No: 00-019-0412, 00-014-0619, and 00-002-1272) The PXRD pattern of the CZTS NCs after 3 h shows a shift in a few peaks with respect to 4 h, which may be due to phase evolution from a mixture of the secondary phase and WZ CZTS to pure WZ CZTS. The results for the as-synthesized CZTS NCs after 4 h confirm the formation of a pure WZ phase based on the gradual evolution of the diffraction planes to that of a single phase. These results are consistent with the literature.[9-11] The combination of kinetic factors is responsible for the formation, growth and stability of the WZ phase NCs.[14, 17] There might be

possible interactions between the metal cations and the glycol that alter the chemical environment and promote the formation of the WZ phase.

The as-synthesized CZTS NCs were further studied using Raman spectroscopy, and the Raman scattering results are shown in Figure 1b. All CZTS NCs synthesized at different reaction time exhibit Raman peaks at 331.7 and 287.8 cm^{-1}, which are the characteristics Raman peaks for WZ CZTS. This result indicates that the characteristic peaks for WZ CZTS may differ from the KS CZTS, which may be caused by the different arrangement of atoms in the space groups of WZ and KS CZTS.[18] In addition to the above-mentioned Raman peaks, the presence of several other peaks of secondary phases, such as $Cu_{2-x}S$, $Sn_{1-x}S_x$ and Cu_2SnS_3 (CTS), are observed for CZTS NCs samples synthesized for 1 and 2 h.[19, 20] The presence of intense peaks at 381.8 and 470.7 cm^{-1} is attributed to the $Cu_{2-x}S$ phase in the NCs synthesized for 1 h.[19] After increasing the reaction time to 2 h, a decrease in the intensities of these peaks is observed, which is due to the phase conversion of $Cu_{2-x}S$ to CTS.[10] This behavior could be due to the possible gradient composition and the dangling the bonds of the surface atoms. As the reaction proceeds for 3 and 4 h, the pure phase is synthesized. The Raman spectrum in Figure 1b, which corresponds to a 4 h synthesis, has the characteristic intense peak at 331.7 cm^{-1} and weak shoulder peak at 287.8 cm^{-1}, indicating the formation of the pure WZ phase.[21, 22]

The morphology of the as-synthesized NCs is strongly dependent on the surfactants and reaction conditions.[23] Different surfactants are able to selectively bind on particular facets, allowing for anisotropic growth.[23] Additionally, the changes in reaction time can lead to different forms of the reaction products, varying from kinetically to thermodynamically favorable.[14] The morphology of the as-synthesized CZTS NCs with different reaction time is investigated using FE-SEM and shown in Figure S2. The presence of many secondary and ternary phases of Cu, Zn, Sn and S with spherical-plate-like mismatched morphology is observed for NCs synthesized for 1 and 2 h.[20] Furthermore, at a reaction time of 3 h, the formation of CZTS with an incomplete-plates-like morphology occurred. With further increase in reaction time up to 4 h, the diameter decreases due to complete phase transition, while retaining the shape leads to the development of pure WZ CZTS nanoplates.

To study the elemental compositions of the CZTS NCs, energy dispersive spectroscopy (EDS) was employed, and the results are shown in Table S1. Table S1 shows the chemical compositions and compositional ratios of Cu/(Zn+Sn), Zn/Sn, and S/(metal) of CZTS NCs synthesized for different reaction times. With increasing reaction time, the Cu/(Zn+Sn) ratio decreases from 2.70 to 0.92, while the Zn/Sn ratio decreases from 2.25 to 1.02. The ideally stoichiometric composition of CZTS is obtained when the reaction time is increased to 4 h. This result is close to the theoretical value of 2:1:1:4. The presence of all of the elements, i.e., Cu, Zn, Sn and S, near the stoichiometric ratio after 4 h is confirmed using SEM-EDS analysis (Figure S3a). All of the elements are distributed homogenously in the case of CZTS NCs synthesized for 4 h.

The absorption data were analyzed and the band gap energy was estimated using the classical relationship between the absorption coefficient (α) and the photon energy (hν):

$$(\alpha h\nu)^2 = \alpha\,(h\nu - E_g) \quad \text{----------} \quad \text{(Eq. (1))}$$

The optical band gap energy is obtained by extrapolating the linear portion of the plot of $(\alpha h\nu)^2$ against hν, as shown in Figure 1c. The observed band gap energy values are 1.94, 1.81, 1.56 and 1.50 eV for NCs synthesized at 1, 2, 3 and 4 h, respectively. The wider band gap energies for the NCs synthesized for 1 and 2 h could be due the presence of secondary phases, which shift the optical absorption edge towards higher energy values.[24] The narrowing of the optical band gap energy upon increasing the reaction time is attributed to the phase evolution to WZ CZTS from these secondary phases. The band gap energy of 1.50 eV for WZ CZTS NCs synthesized for 4 h corresponds well with the previous reports.[9, 10, 11]

The morphologies of the CZTS NCs synthesized for the optimized reaction time of 4 h were investigated using bright-field TEM and are shown in Figure 2. The as-synthesized CZTS NCs are mainly hexagonal nanoplates (Figure 2a, b and e), and the resulting CZTS NCs are approximately 25-150 nm in diameter. (Figure 2d). Lin et al. reported WZ CZTSSe NCs synthesized using OLA and oleic acid with size distribution ranges from 15 to 150 nm using DDT and OLA.[10,25] These results indicated that the size distribution of the WZ-based NCs was fairly narrow because of the use of a high boiling point and long chain organic solvents.[10,25] Indeed, a previous work reported CZTS NCs with sizes in the range of 20 to 50 nm and a narrow size distribution. This approach required large amounts of toxic and expensive organic solvents, which results in an expensive and time-consuming process that has a negative environmental impact.[26] Although relatively monodispersive NCs have been obtained, the use of such toxic organic solvents hinders the commercialization of these methods in the near future. The slightly wide size distribution in our case may be due to the use of a low-boiling-point, short-chain organic solvent as the reaction media.[13] However, the use of non-toxic, eco-friendly EG as the solvent is a key step, which will promote this method for large scale production. The polycrystalline selected area electron diffraction (SAED) pattern (Figure 2c) is indexed using rings from the {001}, {100}, {101}, {102}, {110}, and {112} planes of a WZ CZTS phase, which matches well with the PXRD and Raman results shown in Figures 1a and b. A high-resolution TEM (HR-TEM) image of an individual hexagonal nanoplate (Figure 2f and g) showed lattice fringes with a d-spacing value of 0.33 nm attributed to the {100} plane, which matches the WZ structure.[9] The corresponding fast Fourier transform (FFT) pattern, calculated from the HR-TEM image and shown in Figure 2h, matches well with the peaks indexed to the zone axis of the {001} direction.[27] The X-ray photoelectron spectrometry (XPS) measurement was conducted to study the valence states of all of the four elements in the as-synthesized WZ CZTS NCs at an optimized reaction

time. Figure 3 shows the high resolution XPS analysis, which identifies the presence of Cu 2p, Zn 2p, Sn 3d and S 2p in the CZTS NCs. The spectrum of Cu 2p shows two peaks at 932.75 ($2p_{3/2}$) and 952.5 eV ($2p_{1/2}$) with a splitting of 19.75 eV, which is in good agreement with the standard separation (19.9 eV) of Cu (I).[10,11] The Zn 2p peaks appear at 1022.6 ($2p_{3/2}$) and 1045.65 eV ($2p_{1/2}$) with a split orbit of 23.05 eV, which can be assigned to Zn (II).[10,11] The peaks of Sn 3d show binding energies at 486.15 ($2p_{5/2}$) and 494.55 eV ($2p_{3/2}$) with a split orbit of 8.4 eV, which is in good agreement with the value of Sn (IV).[10,11] The S 2p peaks are located at 161.55 ($2p_{3/2}$) and 162.75 eV ($2p_{1/2}$), which are consistent with the binding energy of sulfur in the sulfide state in CZTS.[10,11]

Growth and Formation Mechanism

Based on the above detailed time-dependent crystallographic evolutions (Figure 1a) and elemental composition development (Table S1), a possible formation mechanism is explained. The formation of the final CZTS NCs occurs through several steps: i) The formation of spherical $Cu_{2-x}S$ (Figure 1a), which is also consistent with the shape of $Cu_{2-x}S$ reported elsewhere.[28, 29] ii) Further uncontrolled diffusion of Zn and Sn, which assists in the growth and shape transformation to irregular intermediate NCs.[10] iii) Finally, the complete nucleate conversion and further growth to well-defined 3D nanoplates. This evolution can be explained as anisotropic growth. The anisotropic growth of plates offers features and functions that are difficult to obtain simply via the size-tuning of spherical nanoparticles because this well-controlled size and shape possess different surface areas and crystallographic facets.[30] The corresponding photographs of reaction solution color evolution are shown in Figure S4.

The high degree of dispersibility of the CZTS NCs may indicate that the surfaces of the nuclei are covered by glycol during the NC formation, which limits the growth of the NCs and stabilizes them against agglomeration. One possible explanation is that the metal ions in the solution are surrounded by dimethylene dioxy bridges (-OCH_2CH_2O-) and form metal chelates, which would then decompose into their corresponding sulfides at certain temperatures in accordance with their ionic product. These chelates help balance the different reactivities of the cations in solution. Thus, during the first 1 h, the metal chelate complexes were thermally decomposed to form spherical $Cu_{2-X}S$ at high concentrations, which can also be confirmed by the smallest solubility-product constant of 2.5×10^{-48}. As the reaction time proceeds, interdiffusion of Zn^{2+} and Sn^{4+} were gradually incorporated into $Cu_{2-X}S$ due to the similar anionic lattices of $Cu_{2-X}S$ and CZTS, which replaced some of the Cu^{+}. This incorporation of Zn^{2+} and Sn^{4+} and replacement of Cu^{+} evolved the chemical composition, which can be confirmed from Table S1. With further increases in reaction time to 3 and 4 h, the diffusion of Zn and Sn reached their theoretical value, and finally, hexagonal CZTS NCs were formed through the evolution of the intermediate NCs.[10] Thus, we can conclude that EG not only assists as an activating agent that induces the formation of $Cu_{2-X}S$ during the nucleation step but also serves as a stabilizer to control the WZ phase during the growth process.

Ink Formulation and Thin Film Preparation

An advantage of colloidal NCs is easy dispersion in non-polar solvents. However, the high volatilities and the toxicities of mostly non-polar solvents, such as toluene or hexanethiol, make it challenging for future commercialization of NCs-based TFSCs.[26] Therefore, an attempt was made by Wang et al.[15] to find more environmentally friendly ink formulations, where the environmentally friendly and safe solvent (ethanol) was used along with ethyl cellulose as a binder. However, it is very difficult to remove the binder completely during the drying process because it decomposes into organic (carbon) impurities in CZTS-NC-based thin films. Thus, our goal is to develop an eco-friendly, binder-free ink formulation method that uses ethanol as an environmentally benign solvent because it evaporates quickly, minimizing the organic impurities in the film.

Ink based on WZ CZTS NCs was prepared and was further used to deposit CZTS absorber layers onto Mo-coated glass substrate using a spin coating method. To obtain the desired thickness, numerous coatings of the NC ink were performed. After each layer was deposited, the substrate was heated on a hot plate in an air at 150 °C for 2 min to evaporate the ethanol. The WZ NCs films were then subjected to annealing in a S vapor atmosphere in a graphite box using an RTA system for 10 min at different temperature ranging from 520 to 580 °C. The corresponding CZTS samples are designated as CZTS-520, CZTS-540, CZTS-560 and CZTS-580. The photographs of an RTA system and a graphite box used for sulfurization process are shown in Figure S5a and c, respectively and the proposed sulfurization process inside a graphite box using RTA system is illustrated schematically in Figure S5b. More details of the ink formulation method and device fabrication can be found in the SI.

Figure 4 shows the surface and cross FE-SEM images of as-deposited (a and f) and sulfurized films at 520 °C (b and g), 540 °C (c and h), 560 °C (d and i), and 580 °C (e and j), respectively. The as-deposited CZTS thin film exhibits a compact, non-porous and densely packed surface morphology. At 520 °C, the sulfurized thin film shows poor grain growth. As the annealing temperature increases, an enhancement of the grain growth is observed. At 560 °C, the film shows compact and superior grain growth. At 580 °C, several voids are observed at the interface between the Mo and the absorber (Figure 4j). Complete grain growth with large grain size is observed in all films except for the film annealed at 520 °C, which is attributed to i) the use of ethanol as the solvent, which can be completely removed during drying process leaving behind no carbon impurities in the film and ii) no pre-processing of the capping ligands, which are very difficult to remove in the washing process. The case of a sulfurized thin-film, bi-layered structure is depicted in Figure 4. The bi-layered structure of the film is due to the formation of MoS_2 at the CZTS/Mo interface. The as-deposited film shows a thickness of 1.23 μm, whereas the sulfurized films show thicknesses of

0.499, 0.540, 0.690 and 0.660 μm, for the CZTS-520, CZTS-540, CZTS-560 and CZTS-580 samples, respectively. The decrease in film thickness after the sulfurization process indicates shrinkage in the material due to decomposition of the organic solvent. In contrast, the increase in the thickness of sulfurized films is attributed to sufficient incorporation of S during sulfurization at higher temperatures.[31] However, with precise control and optimization of the annealing conditions, i.e., S vapor pressure, ramp rate, amount of S and duration of sulfurization, the MoS_2 layer can be eliminated while maintaining a continuous, non-porous, adherent and micrometer-scale film for high performance solar cells. Further studies are underway in this direction in our laboratory.

Figure 5a shows the XRD patterns of the CZTS-520, CZTS-540, CZTS-560 and CZTS-580 samples. It reveals that the hexagonal WZ phase completely disappeared and the tetragonal KS CZTS phase formed for all films after annealing at different temperatures. The XRD patterns of the sulfurized thin films exhibit strong diffraction peaks corresponding to the (112), (220) and (312) planes of a single KS structure. Notably, the diffraction planes corresponding to the KS phase showed a decreased width compared with the WZ NCs, which is consistent with the structure change from WZ to KS after annealing. The peak intensities of the (112) planes in the CZTS thin films increase with increasing sulfurization temperature. The phase transition from WZ to KS is attributed to the energetically preferred reaction.[18] In the KS phase, each cation is bonded to four sulfur anions, and the cation layers alternate with the sulfur anion layer in the crystallographic c-direction, i.e., CuZn/SS/CuSn/SS.[32] In the WZ phase, the surfaces are formed by {100} planes, and the surface atoms have three bonds; however, in KS, the surface is formed by {112} planes, where every atom has three bonds. This result suggests a shift of every third layer of sulfur atoms during the sulfurization process.[33]

Furthermore, Raman analysis was performed to investigate the phase purity and crystal quality of the annealed films as a function of the annealing temperature. Figure 5b shows Raman spectra from the CZTS-520, CZTS-540, CZTS-560 and CZTS-580 samples. The observed Raman peaks of all samples at 287.8, 337.3 and 374 cm^{-1} are in good agreement with the KS phase reported in previous studies.[34-36] No any other peaks are observed, which confirmed the formation of phase pure CZTS at all sulfurization temperatures. In addition, an increase in the crystallinity with the sulfurization temperatures is observed, which can be better understood by comparing the full width at half maximum (FWHM) values calculated from the XRD and Raman results. Figure 5c shows the FWHM values calculated from the XRD peak with the highest intensity and the Raman spectra for the annealed samples. The values of the FWHM from the XRD and Raman spectra in the sulfurized CZTS thin films decreases with increasing sulfurization temperature, indicating superior crystallinity for the annealed samples.

Solar cell performance

Kim et al. reported the first solar cell device with an efficiency of 3.6 % for pure CZTS NCs.[36] However, the use of TPP as a solvent produces highly toxic phosphorus oxides and phosphine fumes, which makes this method cumbersome in terms of future commercialization aspects. Consequently, a polyol mediated synthesis and further CZTSSe device fabrication, exhibiting an efficiency of 2.2 %, was reported by Dong et al. using diethylene glycol as the solvent.[37] In addition to these reports, we reported 2.44 % as the highest PCE for pure CZTS synthesized via a polyol mediated route.

To investigate the effectiveness of our route, solar cell devices incorporating the KS CZTS thin films sulfurized at different temperatures were fabricated. The CZTS solar-cell device was fabricated according to the conventional configuration of glass/Mo/CZTS/CdS/i-ZnO/Al-ZnO as shown in Figure 6a. Details of the device fabrication process are given in the SI. The device shows sharp interfacial layers, indicating that there was no element diffusion during the solar cell fabrication process (Figure 6a). Figure 6b shows the *J–V* characteristics of the CZTS-520, CZTS-540, CZTS-560, and CZTS-580 devices measured under AM 1.5 illumination. During RTA sulfurization, the S vapor pressure produced inside the graphite box is calculated from PV= nRT, the equation for the ideal gas law. Pressures of 0.41, 0.417, 0.423 and 0.438 atm were achieved for the CZTS-520, CZTS-540, CZTS-560 and CZTS-580 samples, respectively. At 0.423 atm (inside the graphite box), the film shows better PCE than the rest.

Upon illumination, the current density and the PCE can be clearly observed to increase with the sulfurization temperature, as shown in Figure 6b. The magnitudes of the short circuit current densities (J_{sc}) are 7.89, 11.0, 12.58, and 11.86 mA/cm^2 for the CZTS-520, CZTS-540, CZTS-560 and CZTS-580 devices, respectively. The corresponding open circuit voltages (V_{oc}) were found to be 0.366, 0.362, 0.471, and 0.446 V, respectively. The increased V_{oc} and J_{sc} for the CZTS-560 device indicate that the electron-hole recombination rate is lower than in the other samples, which is possibly due to the compact, adherent, and void-free morphology with larger grains, which helps the fast transfer of electrons. Although the PCE is enhanced for a specific sulfurization temperature, the J_{sc} value becomes less than those measured for high efficiency (3.6 %) CZTS TFSCs.[36] This result may be attributed to the high series resistance (R_s) and low shunt resistances (R_{sh}) of the device.[38] The relatively low R_{sh} values were due to shorts or leaks through the devices, whereas the high R_s values were due to the formation of thin MoS_2 layers at the Mo/CZTS interface during the sulfurization process.[38] The higher *FF* at precise conditions indicates that the superior morphology of sample CZTS-560 provides efficient transport pathways for electrons with low parasitic losses in the device. As a result, sample CZTS-560 has the highest overall conversion efficiency (η) of 2.44 % compared to the CZTS-520, CZTS-540, and CZTS-580 samples with their respective efficiencies of 1.03, 1.47 and 2.13 %. We also checked the photovoltaic performance of 6 solar cells from each annealing samples, and the results are summarized in Figure S6. Various solar cell parameters obtained for all the devices are presented in Table 1.

For further insight into the devices, external quantum efficiency (EQE) measurements were performed, as shown in Figure 6c. EQE shows an efficiency of approximately 65 % for an optimized absorber layer. In the EQE curve, a long tail decreased gradually from 550 nm, which is attributed to the short minority carrier (electron) diffusion length and the incomplete absorption of light that results from the thin absorber layer.[39] The decrease in the EQE of the device may be due to surface recombination near the p-n junction, incomplete absorption in the absorber region at higher wavelength and the short diffusion length.[21] Further, J_{SC} was also calculated by integrating EQE curve with the standard AM1.5 solar spectrum of 1 sun bias intensity (P_{solar} = 1000 W/m^2). A statistical analysis of the *Jsc* can be found in Table 1. The values are significantly higher than measured in *J-V* curve which may be due to the front grid of the device and the missing EQE data at higher wavelength.[40, 41] Figures 6d and e shows the effect of annealing temperature on the performance characteristics of the solar cell device. As we know, V_{oc} and J_{sc} are comparable with *FF* and η respectively,[42] the increased J_{sc} and *FF* with the temperature are combined to yield a nearly threshold increase in the AM1.5 power conversion efficiency of 2.44 %. The simultaneous improvement in the morphological microstructure can be attributed to the increase in charge carrier mobility. Thus this improved architecture facilitates reduction in *Rs*, leading to the high J_{sc}, V_{oc} and *FF*. Further, at higher temperature it yielded low power-conversion efficiency by cause of low V_{oc} and *FF* due to insufficient interfacial contact. The band gaps of the absorber layers are estimated from the linear extrapolation plot of [hν ln(1-EQE)]^2 vs. (hν), which is as shown in Figure S7. The band gap energy (E_g) values are found to be 1.37, 1.32, 1.40, and 1.47 eV for the CZTS-520, CZTS-540, CZTS-560 and CZTS-580 samples, respectively. The obtained V_{oc} values for CZTS absorber layers at different annealing temperature does not follow the estimated band gap energy values. Generally, it is well known that the CZTS-based TFSCs exhibits V_{oc}-deficient characteristics and the poor values of V_{oc} for CZTS-based TFSCs were strongly related to the high recombination in the p-n junction region due to the high defect density, which can be indirectly estimated using the equation ((E_g/q)-V_{oc}). The values of (E_g/q)-V_{oc} are found to be 1004, 958, 923, and 1024 for the CZTS-520, CZTS-540, CZTS-560, and CZTS-580 samples, respectively. The values of (Eg/q)-V_{oc} are well correlated to the performance of solar cell than those of E_g.

To elucidate the origin of the loss mechanisms in the CZTS TFSCs, the *J-V* characteristics in the dark were measured and analyzed. The dark *J-V* curves were redrawn in three consecutive plots (Figure 7a-c) to determine the diode parameters. The diode parameters, such as shunt conductance (G), series resistance, ideality factor (n_d), and saturation current density (J_o), are analyzed using a lumped circuit model for the solar cells and are shown in Table 2. The values of the shunt conductance (G) were calculated by plotting dJ/dV against V (Figure 7a) and were found to be 2.51, 2.47, 1.3 and 1.7 mS/cm^2 for CZTS-520, CZTS-540, CZTS-560, and CZTS-580 samples, respectively. The shunt conductance calculated for the best solar cells in our case is higher than those of high-efficiency CIGS solar cells (< 1 mS/cm^2).[43]

The current equation of a solar cell device under illumination can be expressed as

$$J = Jo\ \exp[\frac{\mathrm{eV}}{n_d \mathrm{kT}} - 1] \text{ ----------} \quad \text{(Eq. (2))}$$

where J and V are the diode current density and voltage, respectively, J_o is the reverse saturation current density, e is the electronic charge, n_d is the ideality factor, k is the Boltzmann constant, and T is the temperature.[44] Figure 7b shows the r(J) = dV/dJ vs $(J+J_{SC})^{-1}$ plots for the same CZTS devices. The R_s were found to be 2.88, 1.97, 1.40 and 1.78 Ω cm^2 for the CZTS-520, CZTS-540, CZTS-560 and CZTS-580 devices, respectively. These values are higher than those reported by Mitzi et al. for the best CZTSSe solar cells.[2] The most efficient CZTS solar cell device (2.44 %) suffered from a high R_s value, which was caused by the formation of a thin MoS_2 layer at the Mo/CZTS interface during the sulfurization process and the unavoidable impurity phases at the interfaces of the large-grained CZTS absorber and the Mo layer.[45] In contrast, the values of n_d and J_o can improve the understanding of the recombination mechanism in the devices. Furthermore, the J_o values were obtained from the intercept of the linear region of the semi-logarithmic plot $(J+J_{SC})$-GV against V as shown in Figure 7c. The values of J_o are 1.36 x 10^{-5}, 2.63 x 10^{-5}, 8.31 x 10^{-7} and 5.98 x 10^{-7} mA/cm^2 for the CZTS-520, CZTS-540, CZTS-560 and CZTS-580 devices, respectively. This overall decrease in the J_o values may be due to the decreased defect density and carrier recombination. Finally, the n_d values were calculated from the slopes (Slope=n_d=q/AkT) of the semi-logarithmic plots (Figure 7c) and were found to be 2.52, 2.05, 1.68 and 1.93 for the devices based on samples CZTS-520, CZTS-540, CZTS-560 and CZTS-580, respectively. For the CZTS-520 and CZTS-540 devices, the resulting values are greater than the normal values (1< n_d >2). Defects may exist in quasi-neutral region as well at the junctions and are responsible for the carrier recombination at the junction.[46] In contrast, the CZTS-560 and CZTS-580 devices exhibit lower n_d values, which suggest that the recombinations are less than those of the CZTS-520 and CZTS-540 devices. High values of n_d and J_o will decrease the Voc and FF values of a solar cell. Thus, the CZTS-560 device exhibits the best performance in terms of G, Rs, n_d, and J_o, which agrees well with the results from η. Additionally, the photovoltaic performances of the CZTS devices prepared using WZ CZTS NCs were highly reproducible.

Although the efficiency of our solar cell is the highest among the pure CZTS-NC-based devices prepared using a greener, polyol-based synthetic approach, it has a mediocre efficiency compared with the highest efficiency obtained for phase-pure CZTS-NC-based devices. The plausible reasons for the mediocre efficiency are i) the high Rs value; ii) the lack of short circuit current density that results from the poor carrier collection efficiency in the range of 650 to 1100 nm, which results from the presence of voids that lead to the accumulation of defects on the back side of the absorber layer;[47] and iii) the poor nd and high J_o values. Several possible explanations have

been provided for the resulting mediocre efficiency of our pure CZTS-based TFSC. However, more detailed understanding of the NC synthesis and post-annealing conditions is necessary for further improvement in the device performance. This work demonstrates a synergistic attempt at the development of a greener, sustainable and scalable approach for both the synthesis of WZ CZTS NCs and the development of an ink formulation for the fabrication of high-performance CZTS-NC-based TFSCs. This approach is in contrast to the typical route that involves toxic solvents, such as OLA and DDT; toxic disperse solvents, such as toluene and hexanethiol; and a selenization process in a toxic H_2Se gas atmosphere.

Conclusions

We have demonstrated a low-cost, environmentally friendly, and surfactant-free synthesis of pure metastable WZ CZTS NCs via a glycol mediated HI route. Furthermore, a low-cost and eco-friendly binder-free ink formulation method for the preparation of CZTS films was introduced. Time-dependent phase-evolution and the formation mechanism of the WZ-derived CZTS NCs were systematically studied by examining their structural, morphological, and optical properties. Furthermore, the metastable WZ-derived CZTS NCs have been shown to undergo phase-evolution into KS CZTS thin films after annealing in a S atmosphere at temperatures above 500 °C for 10 min. The complete phase-transition and fast grain-growth are closely related to the NC synthesis and ink formulation method. The use of EG, which has a short-carbon chain, as the solvent in the NC synthesis overcomes the problems associated with the washing of capping ligands, which restricts grain growth during the annealing process. In addition, a binder-free ink formulation that utilizes ethanol as the solvent because it evaporates easily during the drying process resulted in large-grained CZTS thin films without any residual C at the CZTS/Mo interface. These results suggest that the solvent used in the NC synthesis and the ink formation play vital roles in the fabrication of a high-quality absorber layer. Our preliminary NC-based TFSCs demonstrated a PCE of 2.44 % without employing toxic Se, which is the highest efficiency achieved for pure CZTS-NC-based TFSCs prepared using a polyol-based hot-injection route. The synthetic strategies developed for the WZ CZTS NC synthesis and their ink formation may have significant potential to be applied in low-cost, high performance solar cells and can be extended to other photovoltaic areas. We believe that this is the first step towards the fabrication of eco-friendly, low-cost and sustainable solar cells.

Acknowledgements

This work is supported by a Human Resources Development (No. 20124010203180) of the Korea Institute of Energy Technology Evaluation and Planning (KETEP) grant funded by the Korea Government Ministry of Trade, Industry and Energy and partially supported by the University Grants Commission, Government of India (No. 41-249 /2012 (SR)).

Electronic Supplementary Information (ESI) available

Experimental details, characterizations, FE-SEM, EDS, photo images of an RTA system, a graphite box and fabricated solar cell device and schematic diagram of sulfurization process, Average photovoltaic performances, Band gap energy plots See DOI: 10.1039/b000000x/

Corresponding Authors

*sskolekar@gmail.com
*jinhyeok@chonnam.ac.kr

Notes and References

1 C. K. Miskin, W. C. Yang, C. J. Hages, N. J. Carter, C. S. Joglekar, E. A. Stach and R. A. Agrawal, Prog. Photovolt. Res. Appl., 2015, 23, 654-659.
2 T. K. Todorov, J. Tang, S. Bag, O. Gunawan, T. Gokmen, Y. Zhu and D. B. Mitzi, *Adv. Energy Mater*. 2013, **3**, 34-38.
3 U. Ghorpade, M. Suryawanshi, S. W. Shin, K. Gurav, P. Patil, S. Pawar, C. Hong, J. H. Kim and S. S. Kolekar, *Chem. Commun.* 2014, **50**, 11258-11273.
4 M. P. Suryawanshi, G. L. Agawane, S. M. Bhosale, S. W. Shin, P. S. Patil, J. H. Kim and A. V. Moholkar, *Mater. Technol*., 2013, **28**, 98-109.
5 C. Leidholm, C. Hotz, A. Breeze, C. Sunderland and W. Ki, NREL Subcontract Report. 2012, NREL/SR-5200–56510.
6 Q. Tian, X. Xu, L. Han, M. Tang, R. Zou, Z. Chen, M. Yu, J. Yang and J. Hu, *CrystEngComm*., 2012, **14**, 3847–3850.
7 P. Kush and S. Deka, *J. Nanopart. Res*. 2014, **16**, 1-14.
8 Y. Qi, Q. Liu, K. Tang, Z. Liang, Z. Ren and X. Liu, *J. Phys.Chem. C,* 2009, **113**, 3939-3944.
9 X. Lu, Z. Zhuang, Q. Peng and Y. Li, *Chem. Commun*., 2011, **47**, 3141–3143.
10 M. Li, W. H. Zhou, J. Guo, Y. L. Zhou, Z. L. Hou, J. Jiao and S. X. Wu, *J. Phys.Chem. C*, 2012, **116**, 26507-26516.
11 A. Singh, H. Geaney, F. Laffir and K. M Ryan, *J. Am. Chem. Soc*., 2012, **134**, 2910–2913.
12 F. J. Fan, L. Wu, M. Gong, G. Liu, Y. X. Wang, S. H. Yu, S. Chen, L. Wang and X. G. Gong, *ACS Nano*, 2013, **7**, 1454-1463.
13 C. Feldmann and H. O. Jungk, *Angew. Chem. Int. Ed*., 2001, **40**, 359-362.
14 Y. L. Zhou, W. H. Zhou, M. Li, Y. F. Du and S. X. Wu, *J. Phys.Chem. C,* 2011, **115**, 19632-19639.
15 C. L. Wang and A. Manthiram, *ACS Sustainable Chem. Eng.,* 2014, **2**, 561−568.
16 O. Zaberca, A. Gillorin, B. Durand and J. Y. Chane-Ching, *J. Mater. Chem.,* 2011, **21**, 6483-6486.
17 Y. H. Wang, A. X. Zhang, N. Bao, B. Lin and A. Gupta, *J. Am. Chem., Soc.,* 2011, **133**, 11072-11075.
18 Z. G. Li, A. L. K. Lui, K. H. Lam, L. F. Xi and Y. M. Lam, *Inorg. Chem.,* 2014, **53**, 10874-10880.
19 P. A. Fernandes, P. M. P. Salomé and A. F. Da Cunha, *Thin Solid Films,* 2009, **517**, 2519-2523.
20 J. M. R. Tan, Y. H. Lee, Pedireddy, T. Baikie, X. Y. Ling and L. H. Wong, *J. Am. Chem. Soc.,* 2014, **136**, 6684-6692.

21 W. C. Yang, C. K. Miskin, C. J. Hages, E. C. Hanley, C. Handwerker, E. A. Stach and R. Agrawal, *Chem. Mater.,* 2014, **26,** 3530-3534.
22 W. Zhang, L. Zhai, N. He, C. Zou, X. Geng, L. Cheng, Y. Dong and S. Huang, *Nanoscale,* 2013, **5**, 8114-8121.
23 K. Ramasamy, M. A. Malik, N. Revaprasadu and P. O'Brien, *Chem. Mater.,* 2013, **18**, 3551-3569.
24 M. Suryawanshi, S. W. Shin, W. R. Bae, K. Gurav, M. G. Kang, G. Agawane, P. Patil, J. H. Yun, J. Y. Lee, A. Moholkar and J. H. Kim, *Phys. Status Solidi (A)*, 2014, **211**, 1531-1534.
25 X. Lin, J. Kavalakkatt, K. Kornhuber, D. Abou-Ras, S. Schorr, M. C. Lux-Steiner and A. Ennaoui, *RSC Adv*., 2012, **2**, 9894-9898.
26 L. Al Juhaiman, L. Scoles, D. Kingston, B. Patarachao, D. Wang and F. Bensebaa, *Green Chem*., 2010, **12**, 1248-1252.
27 Y. Li, Q. Han, T. W. Kim and W. Shi, *Nanoscale,* 2014, **6**, 3777-3785.
28 M. Kruszynska, H. Borchert, J. Parisi and J. Kolny-Olesiak, *J. Am. Chem. Soc*., 2010, **132**, 15976−15986.
29 X. M. Li, H. B. Shen, J. Z. Niu, S. Li, Y. G. Zhang, H. Z. Wang and L. S. Li, *J. Am. Chem. Soc.,* 2010, **132**, 12778−12779.
30 P. R. Sajanlal, T. S. Sreeprasad, A. K. Samal and T. Pradeep, *Nano reviews,* 2011, **2**, 5883-1-62.
31 M. P. Suryawanshi, S. W. Shin, U. V. Ghorpade, K. V. Gurav, G. L. Agawane, C. W. Hong, J. H. Yun, P.S. Patil, J. H. Kim and A. V. Moholkar, *Sol. Energy*, 2014, **110**, 221-230.
32 S. W. Shin, J. H. Han, C. Y. Park, A. V. Moholkar, J. Y. Lee and J. H. Kim, *J. Alloys Compd.,* 2012, **516**, 96-101.
33 R. Mainz, A. Singh, S. Levcenko, M. Klaus, C. Genzel, K. M. Ryan and T. Unold, *Nat. Commun.,* 2014, **5**, 1-10
34 X. Zhang, G. Guo, C. Ji, K. Huang, C. Zha, Y. Wang and N. Bao, *Sci. Rep*., 2014, **4**, 1-8.
35 B. D. Chernomordik, A. E. Béland, D. D. Deng, L. F. Francis and E. S. Aydil, *Chem. Mater.*, 2014, **26** (10), 3191–3201.
36 Y. Kim, K. Woo, I. Kim, Y. S. Cho, S. Jeong and J. Moon, *Nanoscale*, 2013, **5**, 10183-10188.
37 H. Dong, T. Schnabel, E. Ahlswede and C. Feldmann, *Solid State Sci.*, 2014, **29**, 52-57.
38 M. P. Suryawanshi, S. W. Shin, U. V. Ghorpade, K. V. Gurav, C. W. Hong, G. L. Agawane, S. A. Vanalakar, J. H. Moon, J. H. Yun, J. H. Kim and A. V. Moholkar, *Electrochim. Acta*, 2014, **150**, 136-145.
39 A. Cho, S. J. Ahn, J. H. Yun, J. Gwak, S. K. Ahn, K. Shin, H. Song, and K. H. Yoon, *Sol. Energy Mater. Sol. Cells,* 2013, **109**, 17-25.
40 D. M. Berg, R. Djemour, L. Gütay, G. Zoppi, S. Siebentritt and P. J. Dale, *Thin Solid Films*, 2012, **520**, 6291-6294.
41 G. Zoppi, I. Forbes, R. W. Miles, P. J. Dale, J. J. Scragg and L. M. Peter, *Prog. Photovoltaics Res. Appl.,* 2009, **17**, 315-319.
42 M. Law, L. E. Greene, J. C. Johnson, R. Saykally and P. Yang, *Nat. Mater.*, 2005, **4**, 455-459.
43 S. S. Hegedus and W. N. Shafarman, Prog. *Photovoltaics Res. Appl.,* 2004, **12**, 155-176.
44 S. M. Sze, *Physics of semiconductor devices*, Science. 1992, **258**, 1474.
45 J. J. Scragg, T. Kubart, J. T. Wätjen, T. Ericson, M. K. Linnarsson and C. Platzer-Björkman, *Chem. Mater.,* 2013, **25**, 3162-3171.
46 M. A. Green, *Prog. Photovoltaics Res. Appl*., 2003, **11**, 333-340.
47 W. Wang, S. Y. Han, S. J. Sung, D. H. Kim and C. H. Chang, *Phys. Chem. Chem. Phys*., 2012, **14**, 11154-11159.

Journal Name RSCPublishing

ARTICLE

Figure 1. (a) X-ray diffraction (XRD) patterns for NCs synthesized at different reaction time. The presence of multiple phases was observed for reaction times of 1 and 2 h, whereas the formation of pure WZ phase CZTS NCs was observed for 4 h. (b) Raman spectra for NCs synthesized at different reaction times which support the results from XRD. (c) Plot of $(\alpha h\nu)^2$ against hν of NCs synthesized for different reaction times. The band gap energies were found to be 1.94, 1.81, 1.56 and 1.50 eV for 1 h, 2 h, 3 h and 4 h, respectively.

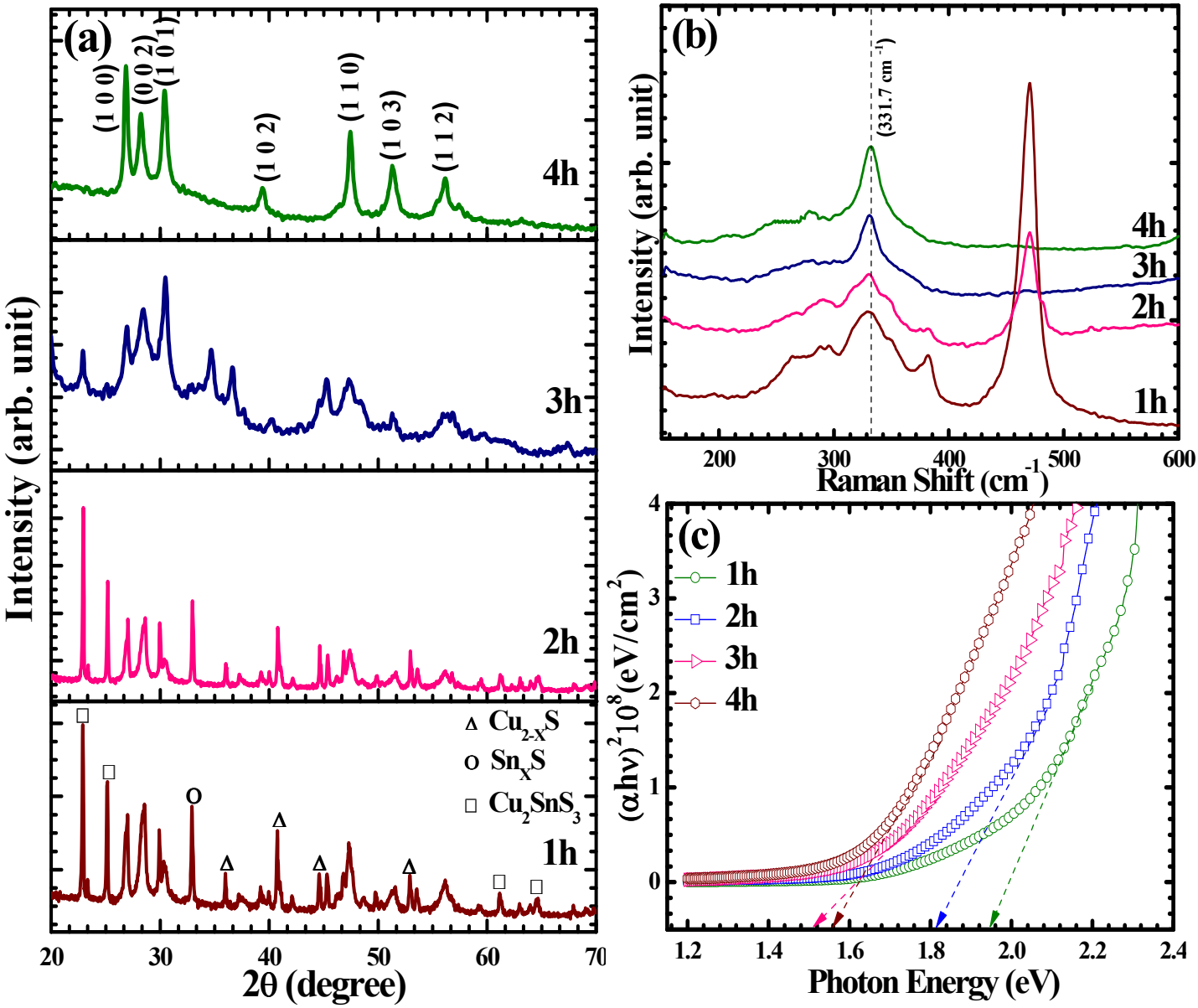

Figure 2. (a) and (b) Bright field TEM images showing the size and shape of WZ-derived NCs synthesized for 4 h. The scale bar is 100 and 50 nm respectively. (c) Selected area electron diffraction (SAED) pattern also support the presence of crystalline CZTS. (d) Size distribution histogram showing the dimensions of WZ-derived CZTS NCs fall in the ranges of approximately 25-150 nm in diameter. (e) Low resolution and (f) and (g) high resolution TEM (HR-TEM) images showing the 0.33 nm of d-spacing for {100} planes. (h) Fast-Fourier transform (FFT) image of the square region in (f) of a WZ-derived CZTS nanoplate which matches well with the peaks indexed to the zone axis of the {001} direction for WZ-derived CZTS NCs synthesized for 4 h.

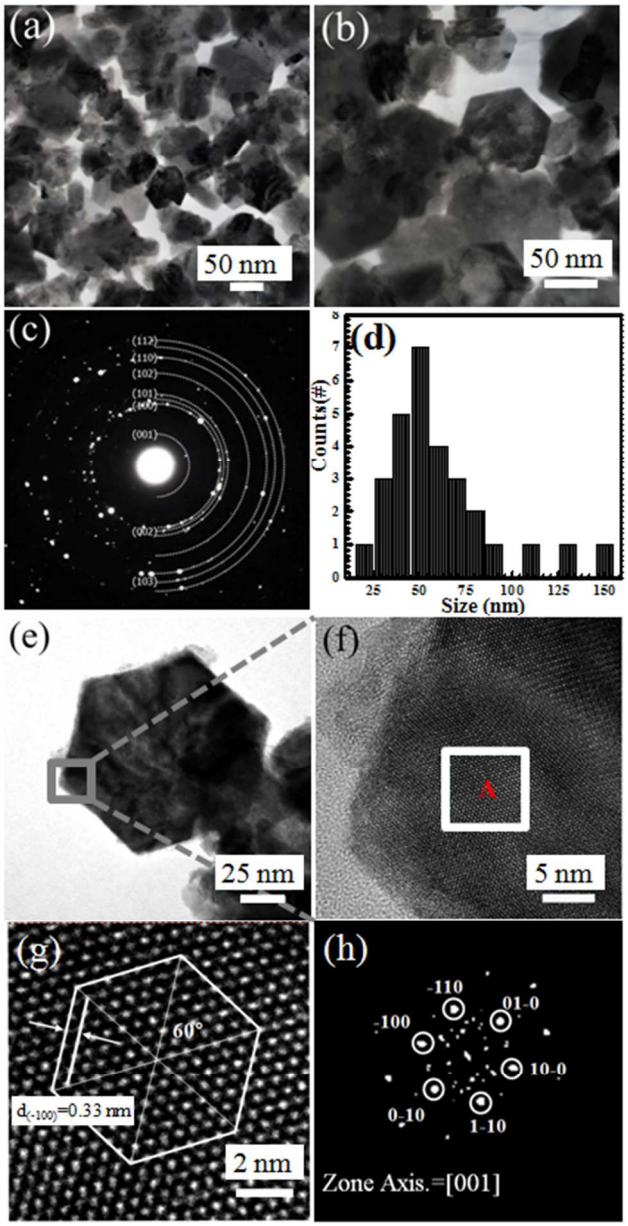

Figure 3. High resolution XPS spectra of WZ CZTS NCs synthesized for 4 h. The presence of all elements was observed for WZ-derived CZTS NCs synthesized for 4 h.

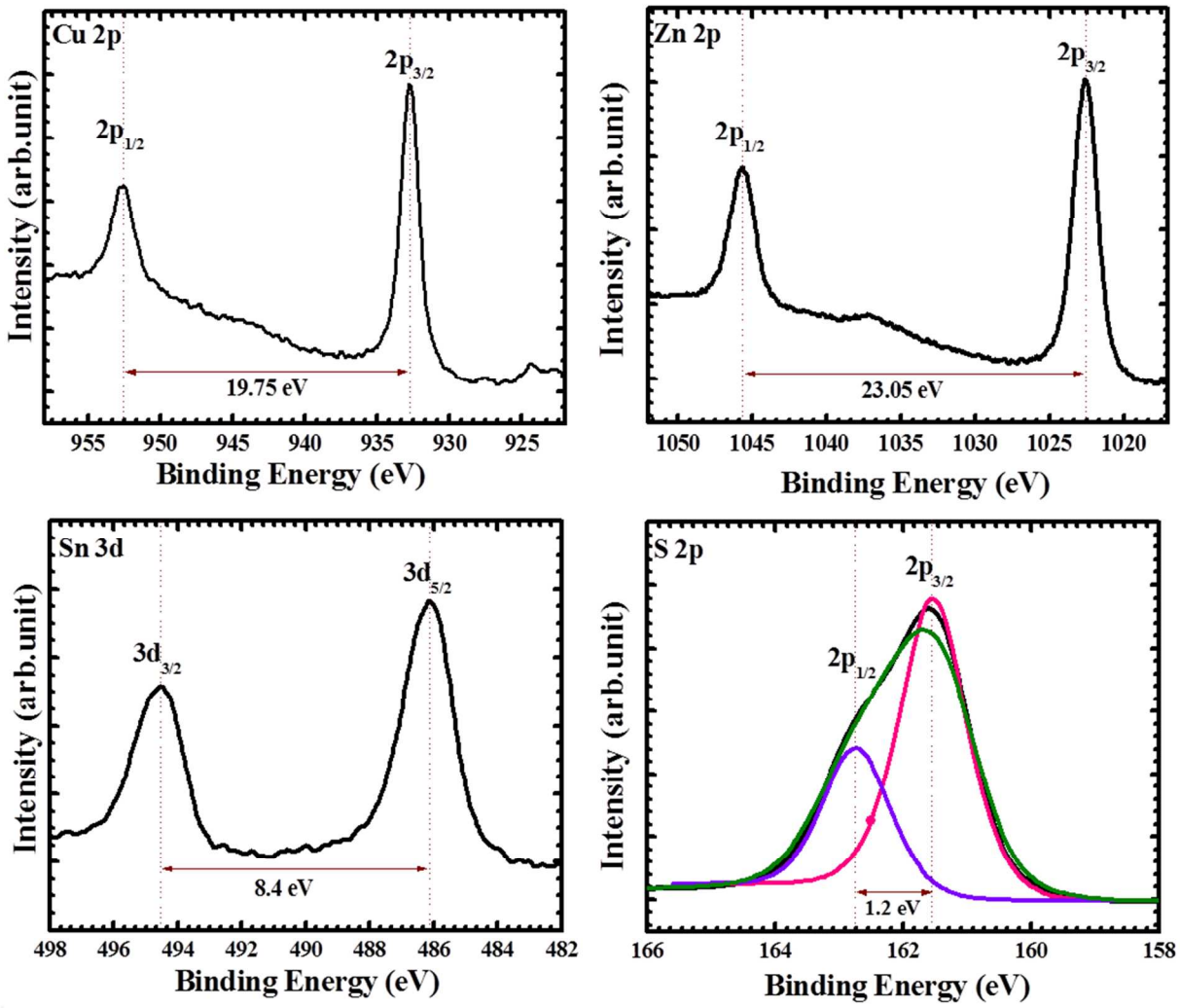

Figure 4. Surface and cross sectional FE-SEM images of as-deposited (a) and (f) and sulfurized films at 520 °C (b) and (g), 540 °C (c) and (h), 560 °C (d) and (i), and 580 °C (e) and (j), respectively. The as-deposited film shows a nanocrystalline surface morphology, whereas the sulfurized films show fully sintered KS CZTS grains after annealing in S vapor atmosphere in a graphite box using an RTA system for 10 min at different temperatures. All scale bars are 1 μm.

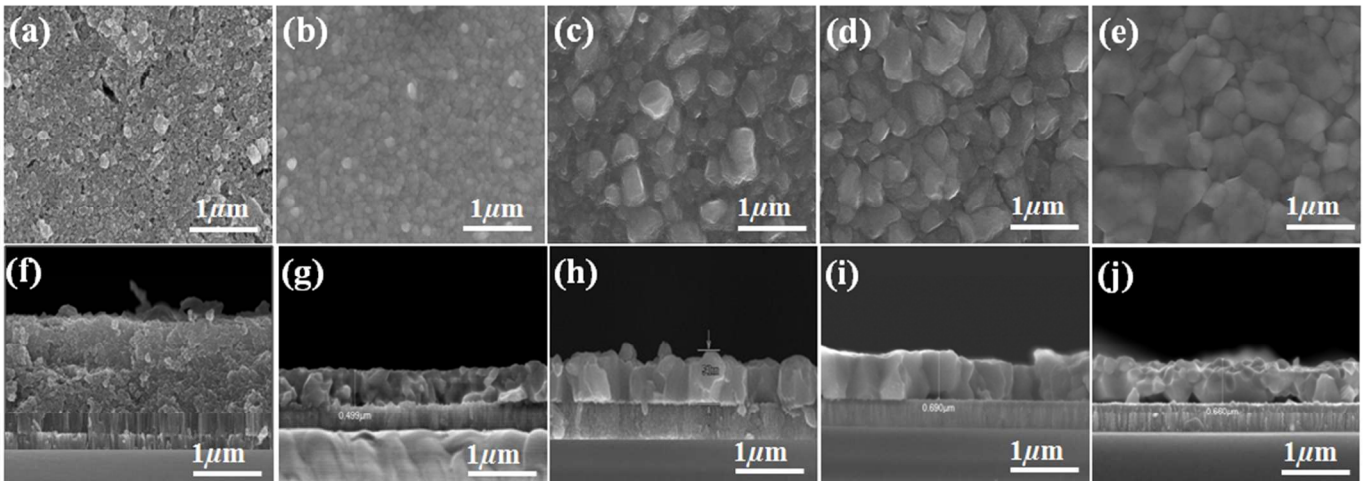

Figure 5. (a) X-ray diffraction (XRD) patterns of the CZTS-520, CZTS-540, CZTS-560, and CZTS-580 samples. Peak marked with asterisks (*) is associated with substrate (~ 40° = Mo). (b) Raman spectra of the CZTS-520, CZTS-540, CZTS-560, and CZTS-580 samples produced by annealing WZ-derived CZTS samples in S vapor atmosphere in a graphite box using an RTA system for 10 min at different temperatures. (c) Variation of FWHM (from the intense peak of XRD and RAMAN) of the CZTS-520, CZTS-540, CZTS-560, and CZTS-580 samples.

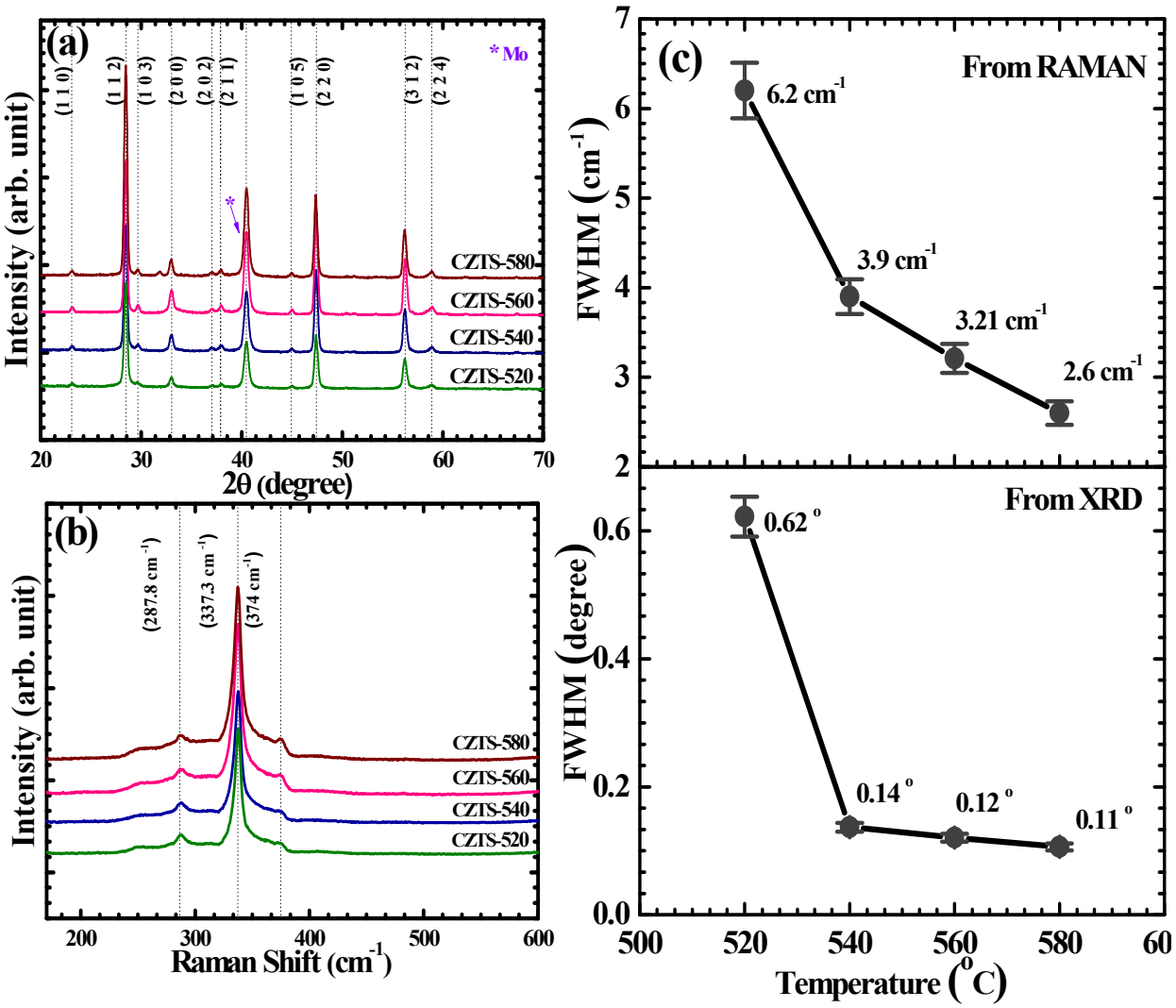

Figure 6. (a) Cross-sectional FE-SEM image of the constitute layers of the optimized CZTS-560 thin film solar cell device. (b) J–V characteristics of best cell from each device under AM 1.5 illumination (c) External quantum efficiency (EQE) recorded in the 300-1200 nm for the CZTS-520, CZTS-540, CZTS-560, and CZTS-580 devices and (d), (e) Open-circuit voltage and fill factor against annealing temperature, and short-circuit current density and efficiency against annealing temperature for the devices with temperature variation between 520- 580 ^{o}C respectively.

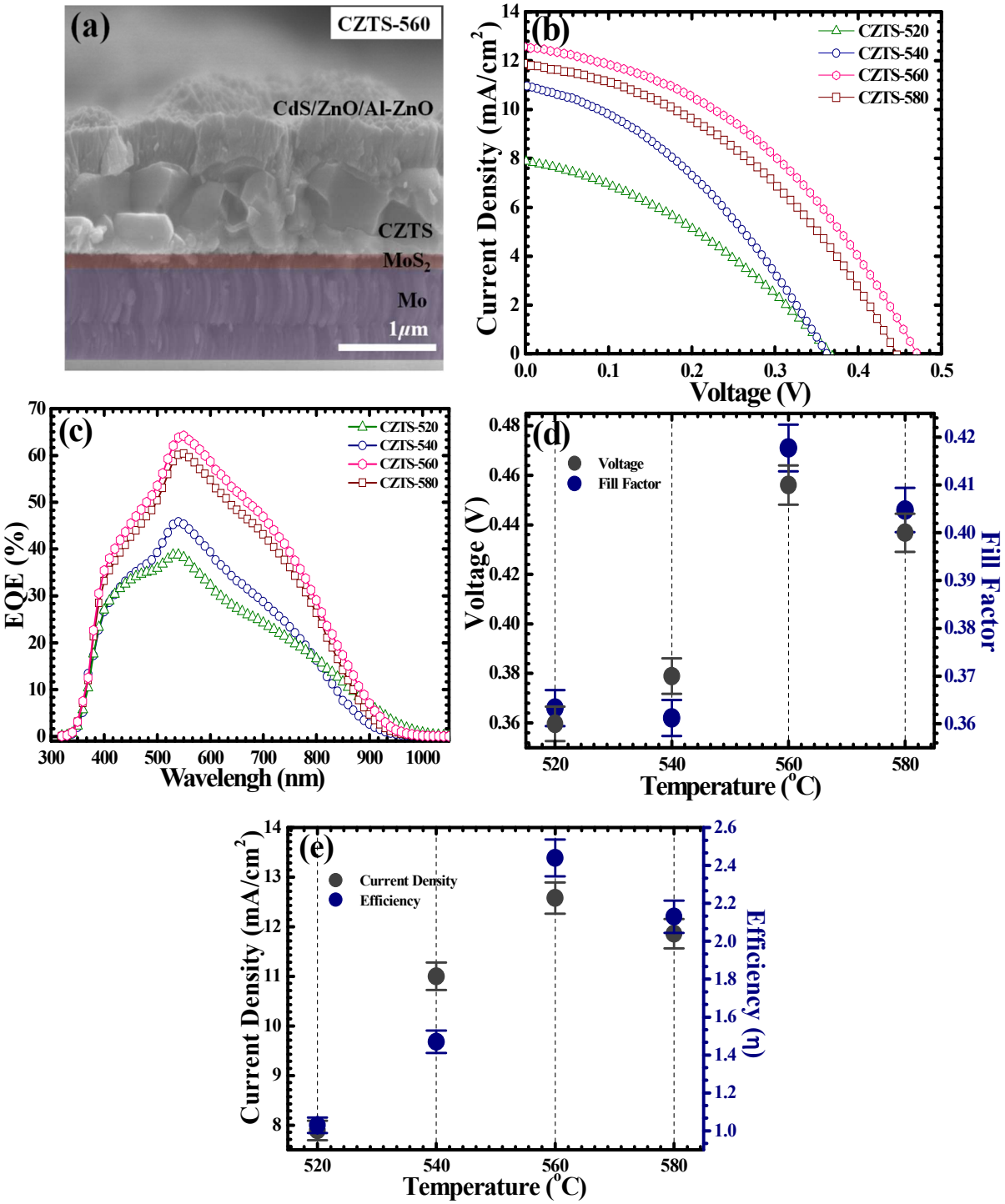

Figure 7. (a) Plots of dJ/dV vs V redrawn from the standard dark J−V curves, where Gsh values were evaluated from the plateau values assuming that an ohmic (shunt) current is predominant over the diode current in this regime. (b) Plots of dV/dJ vs (J + Jsc)−1, where Rs values were extracted from the y-intercepts. (c) Semi-logarithmic plots of J + Jsc−GV vs V−RJ, where J_o and n_d values were extracted from the intercept and slope of the linear region of the curves, respectively.

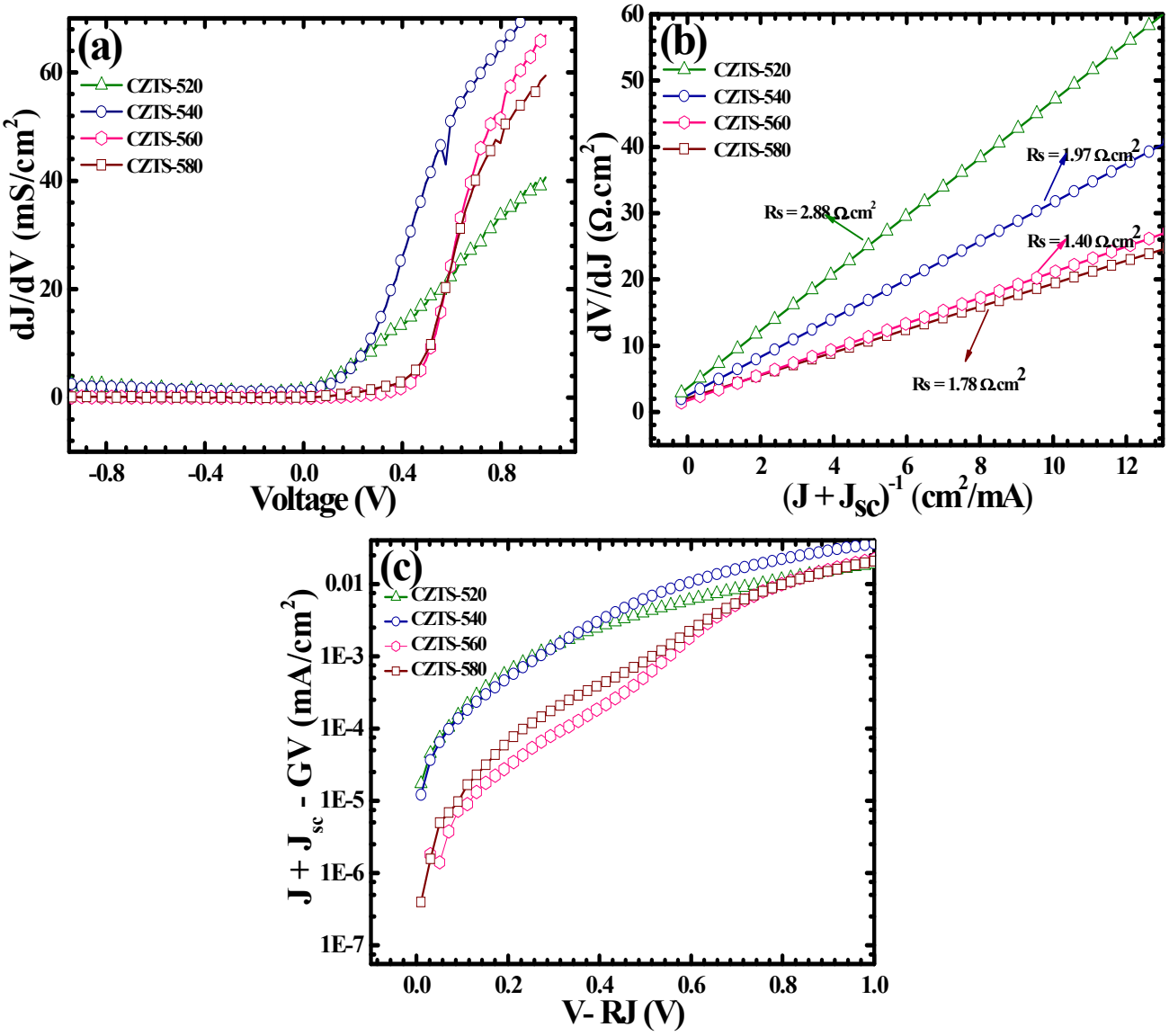

Table 1. Various solar cell parameters from the CZTS-520, CZTS-540, CZTS-560, and CZTS-580 devices

Sample	V_{oc} (V)	J_{sc} (mA/cm^2)	*FF*	Efficiency (%)	Calculated parameters from EQE	
					J_{sc} (mA/cm^2)	E_g (eV)
CZTS-520	0.366	7.89	0.36	1.03	8.5	1.37
CZTS-540	0.362	11.00	0.37	1.47	9.27	1.32
CZTS-560	0.471	12.58	0.41	2.44	14.14	1.40
CZTS-580	0.446	11.86	0.40	2.13	13.02	1.47

Table 2. Typical diode parameters extracted for the CZTS-520, CZTS-540, CZTS-560, and CZTS-580 devices

Sample	G_{sh} (mS/cm^2)	R_s (Ω cm^2)	n_d	J_o (mA/cm^2)
CZTS-520	2.51	2.88	2.52	1.36×10^{-5}
CZTS-540	2.47	1.97	2.05	2.63×10^{-5}
CZTS-560	1.3	1.40	1.68	8.31×10^{-7}
CZTS-580	1.7	1.78	1.93	5.98×10^{-7}